

# **STRESSED PERMEABILITY IN SHALES: EFFECTS OF MATRIX COMPRESSIBILITY AND FRACTURES - A STEP TOWARDS MEASURING MATRIX PERMEABILITY IN FRACTURED SHALE SAMPLES**

Marisa B. Rydzy, Jorge Patino, Nours Elmetni, and Matthias Appel  
Shell International Exploration and Production, Houston, TX

*This paper was prepared for presentation at the International Symposium of the Society of Core Analysts held in Snowmass, Colorado, USA, 21-26 August 2016*

## **ABSTRACT**

To assess how fractures affect the fluid flow in shale plugs, we conducted stress-dependent permeability measurements on both intact and fractured shale samples. We characterized the degree of fracturing with the help of micro X-ray CT images. As expected, permeabilities decreased significantly during the initial effective stress increase. During the subsequent effective pressure decrease, the permeability remained relatively unchanged. The degree of hysteresis depended on the sample integrity, i.e. fracture density, type, and distribution. We recorded an average hysteresis loss of 35% for intact samples, 55% for samples with a low density of hairline or discontinuous mid-sized fractures, and over 75% for samples with thick fractures, high fracture density, or continuous mid-sized cracks. Micro X-ray CT images acquired of fractures subjected to increasing confining stress showed that both, hairline and mid-sized fractures closed up completely at sufficiently high confining pressure. While hairline fractures tended to close at confining pressures as low as 1000 psi, thicker fractures required confining pressures as high as 4000 psi. The results of this study suggest that, as the effect of compressibility of the matrix compared to fractures is relatively small, successful matrix permeability measurements can be conducted even on fractured samples provided a sufficiently high confining pressure is being applied.

## **INTRODUCTION**

Hydrocarbon production lowers the pore pressure which causes an increase in effective stress (overburden or confining stress minus pore pressure) which, in turn, may cause a reduction in the reservoir permeability. Laboratory investigation and characterization of the stress-dependence of permeability represents a key to production forecasting, especially in unconventional shale reservoirs where long-term field production data is not

readily available. Permeability measurements on shale under varying effective stress have been conducted in a number of studies [e.g. Cui and Brezokowski, 2013; Chhatre et al., 2015]. The results of these studies showed that the permeability decreased with increasing confining stress. The permeability decrease generally either followed an exponential [e.g. Kwon et al. 2001; Chalmers et al., 2012; Ghanizadeh et al., 2015] or power law trend [e.g. Dong et al. 2010].

Fluid flow in shales occurs in complex networks of small pores in both mineral matrix and organic matter, as well as fractures. Some fractures are natural. The majority of cracks, however, have been induced by drilling, recovery, and/or core storage. When fractures are present in a shale sample, fluid flow will likely be dominated by the micro-sized openings as they provide less resistance to flow than nano-sized pores. It is thus important to characterize a shale core plug prior to permeability measurements to allow distinction between matrix and fracture flow. In many studies concerned with measuring stressed permeability, the specimen conditions were not specified or well characterized [e.g. Heller et al, 2014; Cao et al. 2016; Ghanizadeh et al. 2015].

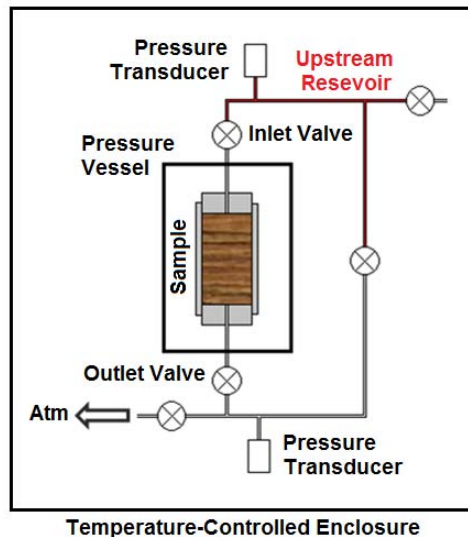
Some studies assessed the sample state based on visual observations, SEM images, or thin sections [e.g. Handwerger et al., 2011; Chalmers et al., 2012]. The condition of the sample surface or a small sub-sample were likely not representative of the condition of the plug used for the permeability measurements. A few recent studies utilized micro X-ray CT imaging to identify fractures in the specimen to be tested. In those studies, fractured studies were omitted from further testing [e.g. Sinha et al. 2013; Cronin et al., 2016]. As fracturing is often a function of core lithology (e.g. TOC content), biased sampling is likely to occur and the sample selection may not completely represent the subsurface formation.

In this study, we systematically performed stress-dependent unsteady-state gas permeability measurements on a number of fractured and a few intact (on MXCT resolution) shale samples. Prior to permeability testing the plugs were imaged with a Micro X-ray CT scanner to characterize density and distribution of the fractures. We then based our interpretation of the stressed-permeability results on the respective sample condition.

## **EXPERIMENTAL SETUP**

Of the many different methods available for plug permeability measurements, i.e. steady-state, pressure-transmission, etc. [e.g. Metwally and Sondergeld 2011; Heller et al., 2014], we chose the pulse-decay method as it was a well-established technique

[Charmers et al. 2012; Cui and Brezokovski, 2013; Cao et al., 2016;]. We conducted these measurements at relatively high pore pressure (1900 psi) as this reduced the duration of the test and practically removed the need to correct for the slip effect. **Figure 1** shows a schematic of the permeameter. The sample is enclosed by an impermeable sleeve and two metal endcaps and submersed in mineral oil inside a pressure vessel. The metal endcaps contain fluid lines through which gas can flow in and out of the sample. The mineral oil acts as confining fluid. The system allows pore and confining pressures of up to 2000 psi and 10,000 psi, respectively. The metal endcaps contain fluid lines through which gas and liquids can flow in and out of the sample. The mineral oil acts as confining fluid and an ISCO pump controls the confining fluid pressure. During the course of a permeability test the confining pressure varies less than  $\pm 3$  psi. Fluid flow in and out of the samples is controlled by an assembly of fluid lines, pneumatic valves, and HIP pumps. DXD pressure transducers record the pressure at the sample inlet and outlet as well as the confining pressure with an accuracy of  $\pm 0.02\%$ . All permeameters are located inside insulated and temperature-controlled enclosure which allows the temperature to remain stable within  $\pm 0.1^\circ\text{C}$  during testing. Experimental data acquisition, display, and the operation of the pneumatic valves are controlled by Metarock®-software.



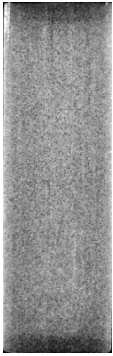
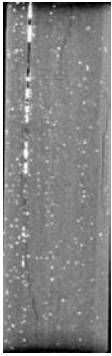

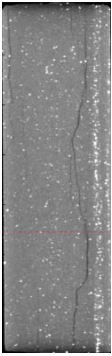
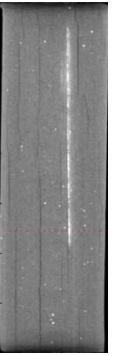
**Figure 1:** Schematic of gas permeameter for shale plugs (not drawn to scale)

## SAMPLE PREPARATION

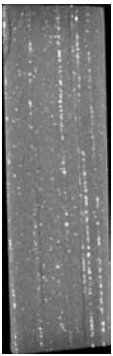
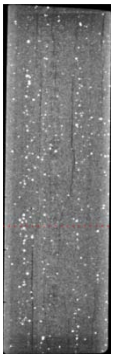
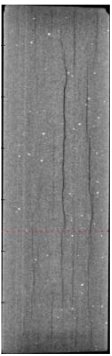

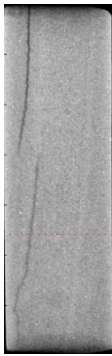
Gas and liquid permeability measurements were performed on gas shale samples from Montney Formation of Western Alberta, Canada. We drilled four horizontal 1-inch diameter plugs from the provided core sections. The plugs were drilled dry with liquid nitrogen as the drilling fluid. They were then scanned with micro X-ray computed

tomography (MXCT) to identify and characterize potential micro-fractures (visible on MXCT scale, ~35 μm). The MXCT images of all 10 samples are shown in **Tables 1-2**. Afterwards, we trimmed the long plugs to a length of about 1 inch. All samples were tested as-received, i.e. with water and organic matter still present in the pore space. The unoccupied pore space was measured with a helium porosimeter (in the following referred to as He porosity). NMR measurements were used to obtain a rough estimate of pore space filled with fluids (in the following referred to as NMR porosity). The total of He and NMR porosity presented a first estimate of the sample's unstressed porosity. **Table 3** lists length, diameter, helium-, and NMR porosity of each sample. Sample length and diameter were measured with a caliper with a precision of ±0.005 cm.

**Table 1:** MXCT Images of Core Samples from Well A (Part 1)

Sample 1 HLC-D-LD	Sample 2 LCX	Sample 3 INTCT	Sample 4 MXC-C/D-LD	Sample 5 HLC-D-HD
				

**Table 2:** MXCT Images of Core Samples from Well A (Part 2)

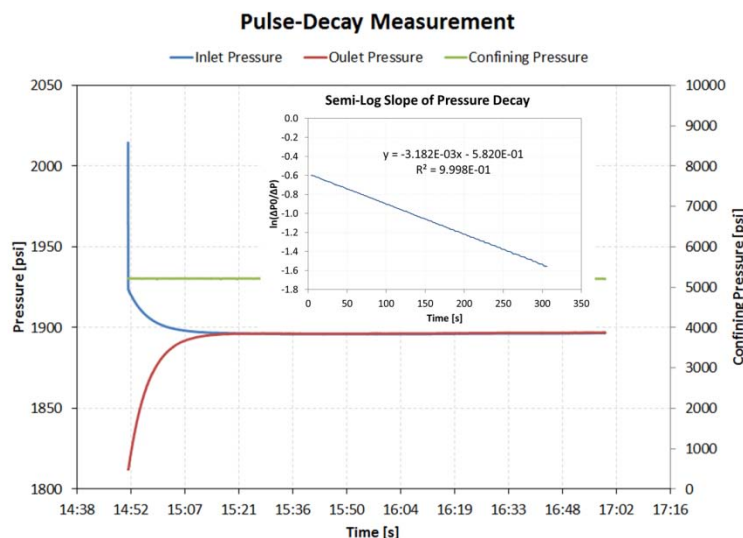
Sample 6 HLC-D-LD	Sample 7 MCX-D-HD	Sample 8 MCX-D-HD	Sample 9 INTCT	Sample 10 MCX-D-LD
				

**Table 3:** Overview of Sample Properties (Total  $\phi$  = He- $\phi$  + NMR- $\phi$ , total apparent porosity)

Sample	L [cm] $\pm 0.01$ cm	D [cm] $\pm 0.01$ cm	He- $\phi$ [%] $\pm 0.5$ p.u.	NMR- $\phi$ [%] $\pm 1.0$ p.u.	Total $\phi$ [%] $\pm 1.1$ p.u.
001	2.79	2.54	2.7	1.9	4.6
002	2.72	2.54	4.1	2.0	6.1
003	2.70	2.54	2.3	2.1	4.4
004	2.57	2.54	4.9	2.1	7.0
005	2.51	2.53	4.6	1.9	6.5
006	2.53	2.56	3.4	1.9	5.3
007	2.66	2.55	4.4	2.0	6.4
008	2.77	2.55	4.4	1.9	6.3
009	2.53	2.54	7.4	2.7	10.1
010	2.66	2.54	4.4	1.9	6.3

## PERMEABILITY MEASUREMENTS

We placed the samples in the permeameter and applied a confining pressure of 2700 psi. Helium was then injected into samples and the pore pressure was raised to 1800 psi. In this study, we used high pore-pressure (1900 psi) pulse-decay tests with helium to determine the permeability of the core plugs. In a pulse-decay test, sample, upstream, and downstream reservoir constitute a closed system. In the beginning of the test, the upstream reservoir (marked in red) is isolated from sample and downstream reservoir, and is charged at a higher pressure than the other two volumes. The pressure of the upstream reservoir was set to 2000 psi and then released through the sample into the downstream reservoir. Both, upstream pressure decrease and downstream pressure increase were recorded as the system reached equilibrium (**Figure 2**).



**Figure 2:** Example of 1900 psi pulse-decay curve recorded for Sample 008 at a confining pressure of 5100 psi. The slope of the normalized logarithm of the pressure difference over time is proportional to the permeability of the sample.

From the pulse-decay curves the permeability of the sample is calculated using the semi-empirical technique presented by Dicker and Smits [1988]. In this method, the slope of the logarithm of the pressure difference between upstream and downstream reservoir (**Figure 2**) is proportional to the apparent gas permeability  $k_a$ , which at a pore pressure of 1900 psi represents a good approximation of the absolute permeability. Nevertheless, the difference between  $k_a$  and  $k_{inf}$  also represents one of our two major sources of uncertainty (the other one being stress creep). The error associated with slip ranged between 5-15%.

During the confining-pressure cycle, the confining pressure was increased from 2700 psi to 3500 psi, and then to 8300 psi in increments of 1600 psi. Afterwards the confining pressure was decreased incrementally back to 2700 psi using the same pressure steps. A pulse-decay test was performed at each pressure step. We waited 24 hours between applying the confining pressure and running a pulse-decay test. The choice of measurement frequency was prompted by our desire to conduct these experiments in a timely manner and to have all samples subjected to the same stress history to be comparative. We recognize that creep can have a strong effect on the stress-dependency of shale samples (Chhatre et al. 2015), which could lead to a systematic over-estimation of our projected matrix permeabilities and represents the second major uncertainty in our measurements.

## RESULTS AND DISCUSSION

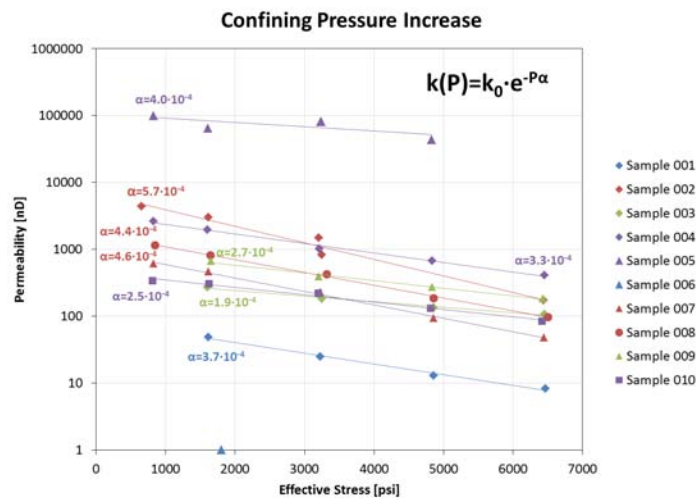
Based on the MXCT scans of the shale plugs (**Tables 1-2**), we assigned a classification to each plug representative of its degree of fracturing. For example, intact samples (on MXCT resolution) were assigned green color coding. Samples with few hairline cracks, a single medium-sized crack, or continuous thick fractures were marked blue, purple, and red, respectively. Details of the fracture classification can be found in **Table 4**.

**Table 4:** Fracture Classification

Color Code	Description
Green	No fractures visible (INTCT)
Blue	Single discontinuous hairline crack (HLC-D-S)
Blue	2-3 discontinuous hairline cracks (HLC-D-LD)
Purple	≥4 discontinuous hairline cracks (HLC-D-HD)
Purple	Single continuous hairline crack (HLC-C-S)
Purple	2-3 continuous hairline cracks (HLC-C-LD)
Red	≥4 continuous hairline cracks (HLC-C-HD)
Purple	Single discontinuous medium-sized crack (HLC-C-S)
Red	2-3 discontinuous medium-sized cracks (HLC-C-LD)
Red	≥4 discontinuous medium-sized cracks (HLC-C-HD)
Red	≥1 continuous medium-sized crack (MCX)
Red	≥1 (dis)continuous large-sized crack (LCX)

At this point of the study the classification was solely based on visual inspection of the MXCT images. The authors recognize that this method may be somewhat subjective as the decision of whether a fracture can be considered thick or thin laid in the eyes of the beholder. In the future, we plan to use more analytical means to make that distinction (e.g. use image analysis software).

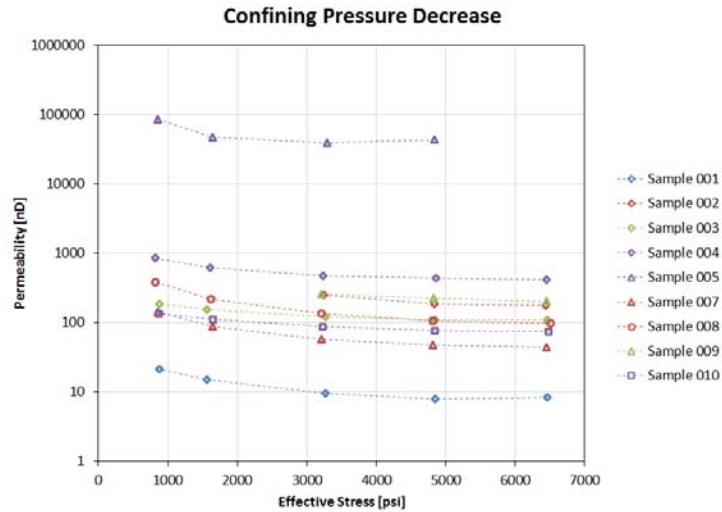
**Figures 3 and 4** show the permeabilities of all the plugs as functions of increasing and decreasing confining stress, respectively. In our study, the permeability decrease generally followed an exponential trend, which manifested itself as a straight line in the semi-logarithmic plot. The lines appear to be parallel for samples with the same color coding indicating that samples with similar degrees of fracturing may exhibit similar compaction behavior. This behavior is also reflected in the slope  $\alpha$  of the exponential function (**Figure 3**). Relatively low values for  $\alpha$  ( $<3.0 \cdot 10^{-4}$ ) were recorded for “intact” samples while relatively high values for  $\alpha$  ( $>4.4 \cdot 10^{-4}$ ) were recorded for heavily fractured samples. During the subsequent confining pressure reduction, the permeability values remained relatively stable (**Figure 4**). Once we reduced the confining stress to pressures below reservoir effective stress of around 3300 psi, the permeability did increase but only slightly. This behavior seems to indicate that once fractures close they do not reopen until the effective stress falls below reservoir conditions.



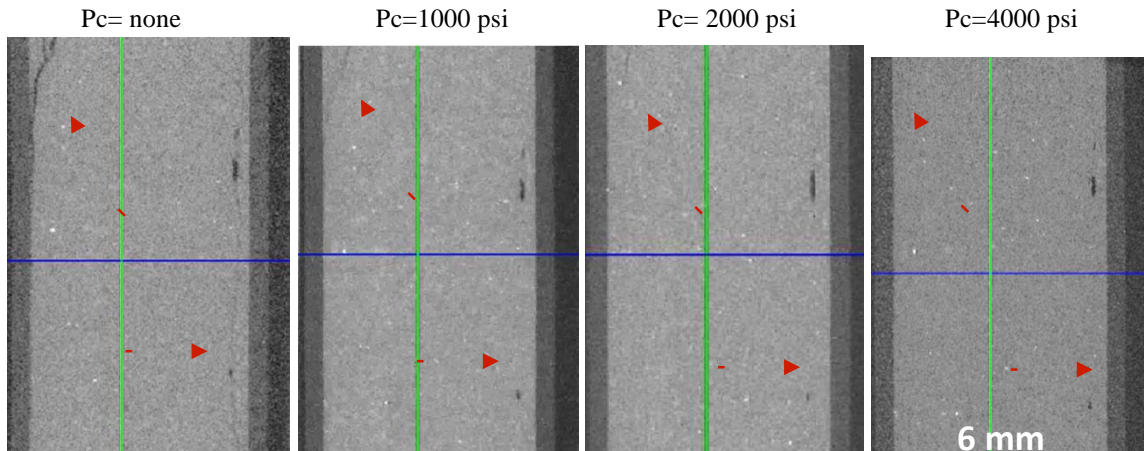
**Figure 3:** Permeability as function of effective stress during confining pressure increase. The slope of the permeability decreases with increasing confining pressure and degree of fracturing.

We acquired MXCT of a fractured 0.6-cm diameter Vaca Muerta shale plug at varying confining stress (**Figure 5**). The image acquired at 0 psi effective stress showed that the small plug contained a medium sized fracture running diagonally across the top and a

lateral hairline fracture. The thin hairline fracture disappeared when we applied an effective stress of 1000 psi, which was below reservoir effective stress. The thicker fracture at the top required us to exceed reservoir effective stress before it closed, i.e. disappeared from the MXCT image. At this point in the investigation, we have not yet acquired the MXCT images during the confining pressure release and thus not yet able to confirm at which pressure the fractures reopen.



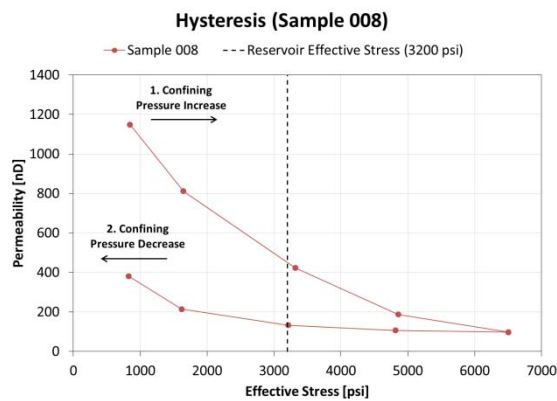
**Figure 4:** Permeability as function of effective stress during confining pressure decrease. Values remain relatively unchanged at effective stresses greater than reservoir conditions (~3300 psi).



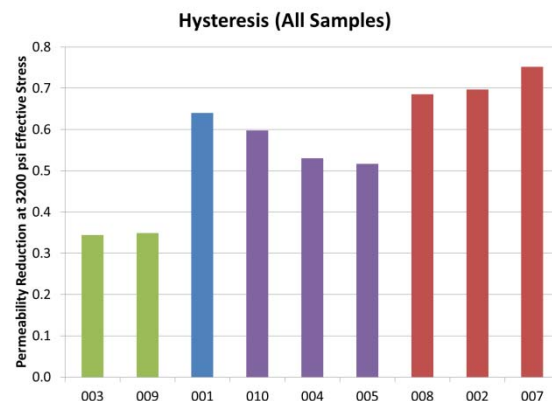
**Figure 5:** MXCT image of fractures in 0.6-cm diameter Vaca Muerta shale plugs under varying confining pressure (no pore pressure was applied). The hairline fracture at the right disappeared after the first pressure step. The thicker crack in the top left corner was closed and no longer visible at 4000 psi confining pressure.



**Figure 6** shows an example of permeability recorded during the increase and decrease in effective stress. The relative difference between the permeability recorded during the confining pressure increase at an effective stress of 3200 psi and the permeability recorded during the confining pressure decrease at the same stress for all samples is depicted in **Figure 7**. As can be seen, for samples that had been classified as “intact” (green), the average hysteresis loss was about 35%. For samples with a low density of hairline or discontinuous mid-sized fractures the average hysteresis loss ranges around 50-60%. For samples with thick fractures, a high fracture density, or a continuous mid-sized crack (red), the average hysteresis loss was around 70% and above. Sample 001 and Sample 010 exhibit slightly higher relative permeability reduction than other samples with a similar degree of fracturing. Sample preparation and handling after the MXCT scans had been acquired may have resulted in additional cracks and caused their deviation from the general trend.



**Figure 6:** Example of permeability data recorded for Sample 008 during initial increase and subsequent decrease in effective stress and the resulting hysteresis



**Figure 7:** Hysteresis observed for different degrees of fracturing

MXCT images and permeability data suggest that the stress-dependence of the permeability in our shale samples is dominated by the fractures. Assuming thusly that the pore compressibility plays a minor role, we might be able to estimate the matrix permeability by a) exposing the samples to sufficiently high stress where all fractures are closed or b) by extrapolating an appropriate fit of our data to sufficiently high pressures where the permeability becomes stable. Our study, as well as most previous studies, recorded shale permeability at relatively low pressures and reported stress-dependencies that followed exponential trends. Dong et al. [2010] reported permeability for stresses up to 120 MPa (17000 psi). Their stress-permeability relationship was best matched by a power function. In this study, we matched our data using Equation 1 below, where  $\Delta P$  is

the pressure increment of 1600 psi,  $P_0$  represents the initial pressure point at which the matched curve is anchored,  $A$  is a fitting parameter which corresponds to a factor by which the permeability reduction ( $\Delta k = k(P - \Delta P) - k(P)$ ) decreases.

$$k(P_0 \pm n \cdot \Delta P) = k(P_0) \mp \left[ \sum_{i=1}^n \frac{k(P_0 - \Delta P) - k(P_0)}{A^i} \right] \quad (1)$$

**Figure 8** shows examples for data fit and extrapolated with Equation 1. The fitting parameters projected matrix permeability values for most samples are listed in **Table 5**. Note that a proper fit could not be found for all samples. Finding a good fit was especially challenging for some samples with a higher degree of hysteresis.

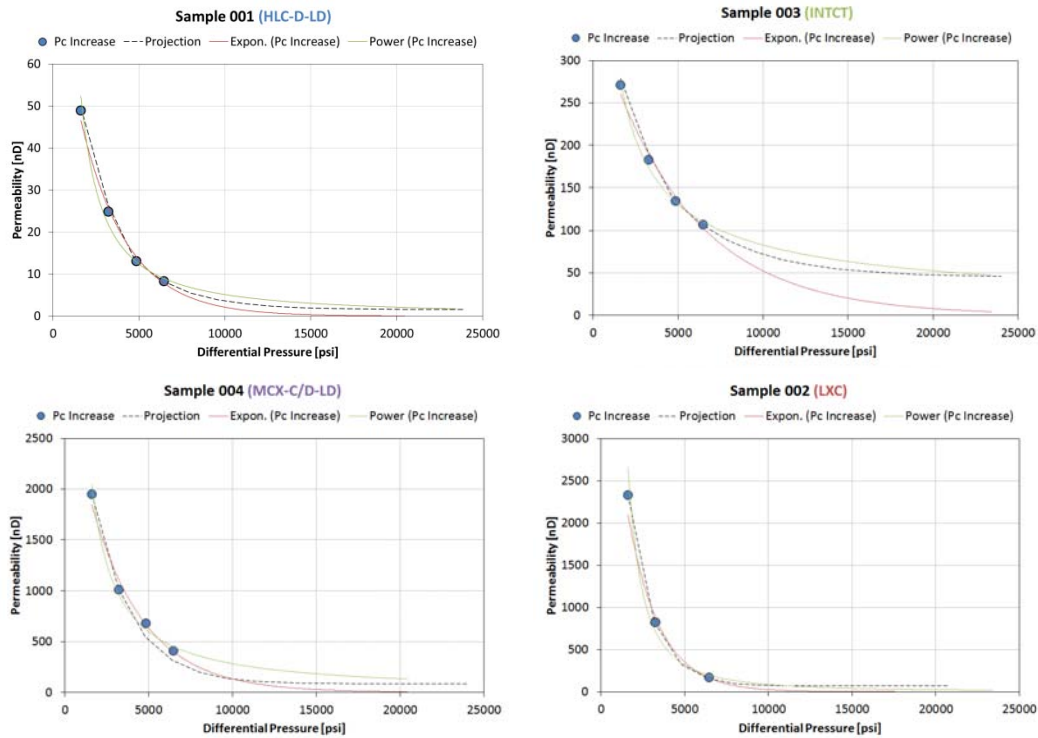
**Table 5:** Fitting Parameters and Projected Matrix Permeability

Sample	$P_0$ [psi]	A	k [nD]	Condition
001	6400	1.70	2	HLC-D-LD
002	3200	3.00	71	LCX
003	6400	1.45	46	INTCT
004	3200	1.6	298	MCX-C-LD
005	No good fit			HLC-D-HD
006	No projection – only 1 data point collected			
007	3200	2.00	1	MCX-D-HD
008	No good fit			MCX-D-HD
009	3200	2.00	113	INTCT
010	No good fit			MCX-D-LD

## CONCLUSIONS

In this study, we demonstrated the importance of sample characterization prior to permeability measurements. Based on our measurement results, we hypothesized that the compaction behavior of shale permeability may be largely dominated by micro-fractures present in the rock samples. Samples with similar degrees of fracturing exhibited similar stress-permeability relationships. With increasing confining stress, fractures close and permeability decreases. In this and other similar studies these stress-permeability relationships exhibited exponential trends at effective stresses smaller than 6,000 psi but may be better represented by power functions at higher stresses. We presented an equation that honors the initial exponential permeability decay but predicts permeability stabilization at higher pressures, somewhat similar to the power function. Under the assumption that the pore compressibility plays a minor role, application of high effective stresses or extrapolation of “low-pressure” stress-permeability data allows us to estimate matrix permeability even for fractured samples, which may reduce some of the bias often encountered in shale plug sampling. Note that our conclusions were drawn based on the results of measurements on a limited number of samples from one single well. Additional measurements will have to be conducted on samples from other wells and formations to

support our hypothesis. In addition, the stress-dependent permeability should be viewed in context with lithological information as other rock properties, such as mineralogy, TOC, and porosity may also impact shale compaction. These issues will be addressed in future research.



**Figure 8:** Permeability as function of effective stress matched with 1) exponential function, 2) power law, and 3) using Equation 1 for 4 samples with different fracture characteristics

## ACKNOWLEDGEMENTS

We would like to acknowledge Irma Eggenkamp, Liya Zhang, and Felix Todea who provided us with samples. This research was funded by the Groundbirch Area Team. The MXCT images of the Vaca Muerta mini-plugs were acquired by Dmitry Shaporov, and the rock material scanned was provided by Melanie Durand and the Vaca Muerta Team. The NMR measurements were conducted at Shell by Ben Anger.

## REFERENCES

Cao, C., T. Li, J. Shi, L. Zhang, S. Fu, B. Wang, and H. Wang (2016), A new approach for measuring the permeability of shale featuring adsorption and ultra-low permeability, *Journal of Natural Gas Science and Engineering*, doi:10.1016/j.jngse.2016.02.015

- Charmers, G.R.L., D.J.K. Ross, and R.M. Bustin (2012), Geological controls on matrix permeability of Devonian Gas Shales in the Horn River and Liard basins, northeastern British Columbia, Canada, *International Journal of Coal Geology* 103, 120-131
- Chhatre, S.S., E.M. Braun, S. Sinha, M.D. Determan, Q.R. Passey, T.E. Zirkle, A.C. Wood, J.A. Boros, D.W. Berry, S.A. Leonardi, and R.A. Kudva (2015), Steady-State Stress-Dependent Permeability Measurements of Tight Oil-Bearing Rocks, *Petrophysics* 56 (2), 116-124
- Cronin, M.B., P.B. Fleming, and A.R. Bhandari (2016), Dual-permeability microstratigraphy in the Barnett Shale, *Journal of Petroleum Science and Engineering* 142, 119-128
- Cui, A., and R. Brezovski (2013), Laboratory Permeability and Diffusivity Measurements of Unconventional Reservoirs: Useless of Full Information? A Montney Example from the Western Canada Sedimentary Basin, SPE 161747
- Dicker, A.I., and R.M. Smits (1988), A Practical Approach for Determining Permeability From Laboratory Pressure-Pulse Decay Measurement, SPE 17578
- Dong, J.J., J.Y. Hsu, W.J. Wu, T. Shimamoto, J.H. Hung, and E.C. Ye (2010), Stress-dependence of the permeability and porosity of sandstone and shale from TCDP Hole-A, *International Journal of Rock Mechanics and Mineral Science* 47, 1141-1157
- Ghanizadeh, A., S. Bhowmik, O. Haeri-Ardakani, H. Sanei, C. R. Clarkson (2015), A comparison of shale permeability coefficients derived using multiple non-steady-state measurement techniques: Examples from the Duvernay Formation, Alberta, *Fuel* 140, 371-387
- Handwerger, D.A., R. Suarez-Rivera, K.I. Vaughn, and J.F. Keller (2011), Improved Petrophysical Core Measurements on Tight Shale Reservoirs Using Retort and Crushed Samples, SPE 147456
- Heller, R., J. Vermylen, and M. Zoback (2014), Experimental investigation of matrix permeability of gas shales, *AAPG Bulletin* 98 (5), 975-995
- Kwon, O., A.K. Kroneberg, A.F. Gangi, and B. Johnson (2001), Permeability of Wilcox shale and its effective pressure law, *Journal of Geophysical Research*. 106, 19339-19353
- Metwally, Y.M., and C.H. Sondergeld (2011), Measuring low permeabilities of gas-sands and shales using a pressure transmission technique, *International Journal of Rock Mechanics & Mining Sciences* 48, 1135-1144
- Sinha, S., E.M. Braun, M. Determan, and Q.R. Passey, S.A. Leonardi, J.A. Boros, and R. Kudva (2013), Steady-State Permeability Measurements on Intact Shale Samples at Reservoir Conditions – Effect of Stress, Temperature, Pressure, and Type of Gas, SPE 164263